ADVANCED
SCIENCE NEWS
www.advancedsciencenews.com

NANO MICRO
small

Li-Ion Batteries

Molecular-Level Design of Hierarchically Porous Carbons Codoped with Nitrogen and Phosphorus Capable of In Situ Self-Activation for Sustainable Energy Systems

Wei Ai, Xuewan Wang, Chenji Zou, Zhuzhu Du, Zhanxi Fan, Hua Zhang, Peng Chen, Ting Yu,* and Wei Huang*

Hierarchically porous carbons are attracting tremendous attention in sustainable energy systems, such as lithium ion battery (LIB) and fuel cell, due to their excellent transport properties that arise from the high surface area and rich porosity. The state-of-the-art approaches for synthesizing hierarchically porous carbons normally require chemical- and/or template-assisted activation techniques, which is complicate, time consuming, and not feasible for large scale production. Here, a molecular-level design principle toward large-scale synthesis of nitrogen and phosphorus codoped hierarchically porous carbon (NPHPC) through an in situ self-activation process is proposed. The material is fabricated based on the direct pyrolysis of a well-designed polymer, melamine polyphosphate, which is capable of in situ self-activation to generate large specific surface area (1479 m^2 g^{-1}) and hierarchical pores in the final NPHPC. As an anode material for LIB, NPHPC delivers a high reversible capacity of 1073 mAh g^{-1} and an excellent cyclic stability for 300 cycles with negligible capacity decay. The peculiar structural properties and synergistic effect of N and P codopants also enable NPHPC a promising electrocatalyst for oxygen reduction reaction, a key cathodic reaction process of many energy conversion devices (for example, fuel cells and metal air batteries). Electrochemical measurements show NPHPC a comparable electrocatalytic performance to commercial Pt/C catalyst (onset potential of 0.88 V vs reversible hydrogen electrode in alkaline medium) with excellent stability (89.8% retention after 20 000 s continuous operation) and superior methanol tolerance.

W. Ai, Z. Du, Prof. W. Huang
Key Laboratory of Flexible Electronics (KLOFE) &
Institue of Advanced Materials (IAM)
Jiangsu National Synergetic Innovation Center for Advanced
Materials (SICAM)
Nanjing Tech University (NanjingTech)
30 South Puzhu Road, Nanjing 211816, China
E-mail: iamwhuang@njtech.edu.cn

W. Ai, C. Zou, Prof. T. Yu
Division of Physics and Applied Physics
School of Physical and Mathematical Sciences
Nanyang Technological University
Singapore 637371, Singapore
E-mail: yuting@ntu.edu.sg

Dr. X. Wang, Prof. P. Chen
School of Chemical and Biomedical Engineering
Nanyang Technological University
70 Nanyang Drive, Singapore 637457, Singapore

Dr. Z. Fan, Prof. H. Zhang
Center for Programmable Materials
School of Materials Science and Engineering
Nanyang Technological University
Singapore 639798, Singapore

Prof. T. Yu
Department of Physics
Faculty of Science
National University of Singapore
Singapore 117542, Singapore

Prof. W. Huang
Key Laboratory for Organic Electronics &
Information Displays (KLOEID) and
Institute of Advanced Materials (IAM)
SICAM
Nanjing University of Posts & Telecommunications
Nanjing 210023, Jiangsu, China

1. Introduction

Increasing energy and environmental concerns promote urgent demand for clean, reliable and affordable energy technologies.[1] Electrochemical energy storage and conversion devices, such as lithium ion batteries (LIBs), metal–air batteries, and fuel cells, have been particularly developed.[2,3] However, these presently available energy devices cannot satisfy the emerging market demands (e.g., electric vehicles and large-scale smart grids) due to their limited charge storage capability and energy conversion efficiency and rate. Electrochemical performance of energy devices is determined in a large extent by their active electrode materials which directly participate in or indirectly catalyze electrochemical reactions. Accordingly, multivalent transition metal oxides/sulfides/hydroxides and electrocatalytically active precious metal nanostructures have been prepared for diverse applications in electrochemical energy systems.[4–7] However, inorganic nanostructures generally suffer from poor conductivity and/or instability in electrochemical process. Transition metal oxides, for example, offer high theoretical capacity for Li ion storage but suffer from irreversible phase transition specifically at high lithiation/delithiation rates. This will severely shorten the lifetime of batteries. Cathodic oxygen reduction reaction (ORR) is a pivotal but rate-limiting step in many sustainable energy conversion systems, for example, metal–air batteries and fuel cells. Platinum (Pt) has been considered as the most effective catalyst to promote ORR at the cathode, however, its practical application has always been plagued by high cost, poor durability, and the susceptibility to fuel and CO poisoning.

In recent years, nanostructured carbon materials (e.g., graphene, carbon nanotubes, carbon nanofiber, and porous carbon) have received intensive research interests in energy storage and conversion applications owing to their exceptional physicochemical properties and low cost.[8–11] However, pristine carbon nanomaterials lack intrinsic chemical and electrochemical activities. Fortunately, doping heteroatoms (e.g., B, N, S, P, and halogen) into carbon lattices could cause structural and electronic modulation, which gives rise to carbon nanomaterials new properties and application opportunities in energy field.[12] In particular, the binary- and multidoping of foreign atoms (e.g., N–P, N–S) into carbon nanomaterials reveal significant synergistic effect on boosting their electrochemical activities.[8,13–15] Despite the remarkably improved performances touted in many cases, heteroatom doped carbon nanomaterials are far from practical application due to their expensive/complex synthesis procedure and low productivity.[16,17]

Organic chemistry enables rational and cost-effective fabrication of multifarious precursors for carbon-based materials that contain specific heteroatoms. As a result, various heteroatom doped carbonaceous nanostructures, such as N,P-codoped porous carbon,[18,19] N-doped porous carbon[20,21] and S-doped porous carbon,[22,23] have recently been prepared via direct pyrolysis of polymer precursors. However, such process usually faces an insuperable impediment to pore collapse, resulting in lack of hierarchical pores in the final bulk carbon products. It is worth pointing out that hierarchically porous structures benefit for providing rich active sites for electrochemical reactions and efficient pathways for ion transport. To create hierarchical porosity, the most applicable approach involves a chemical (e.g., KOH and ZnCl$_2$) or template (e.g., silica and zeolite) assisted activation process, which is quite complicated and time consuming.[24,25] Moreover, from a practical point of view, it is also not feasible for large scale production. Therefore, developing efficient and scalable synthesis techniques for rational fabrication of advanced heteroatom doped porous carbon nanostructures is highly desirable yet remains challenging.

Here, we report molecular-level design and fabrication of nitrogen and phosphorus codoped hierarchically porous carbon (NPHPC), simply by pyrolysis of melamine polyphosphate (MPP, chemical structure shown in **Figure 1**A) synthesized via a facile organic approach by using low cost industrial raw materials (melamine and polyphosphoric acid (PPA)). In this well-designed MPP precursor, melamine serves as the C and N sources for NPHPC, whereas PPA functions as both the P source and a potent scaffold for melamine cross-linking. Simultaneously, PPA affords in situ self-activation for easy formation of high surface area and abundant porous structures during pyrolysis.[26,27] In sharp contrast to conventional chemical reagent activation and template approaches for producing hierarchically porous carbons,[28,29] our protocol involves in situ self-activation, thus avoiding the troublesome postprocessing that always comes with corrosive chemicals and template materials. The resulting NPHPC possesses hierarchical micropores, mesopores and macropores, and a large specific surface area. As a proof-of-concept demonstration, we show the exceptional performance of NPHPC as anode material for LIB and electrocatalyst for ORR, which highlight the huge potential of NPHPC for future sustainable energy systems. With the merits of facile, low cost and scalable features, our strategy will be useful in a practical point of view.

2. Results and Discussion

2.1. Material Design and Characterization

NPHPC fabrication first involves a facile chemical reaction between melamine and PPA to form MPP precursor (Figure 1A), followed by pyrolysis of MPP at a predetermined temperature under argon atmosphere. During the thermal treatment, oligopoly phosphates are initially polycondensed to generate high molecular weight MPP, which undergoes further carbonization to achieve NPHPC. With annealing temperature increasing from 700 to 900 °C, the color of resulting NPHPC changes from gray to black (Figure S1, Supporting Information). The obtained products are denoted as NPHPC-T (T is the pyrolysis temperature). For comparison, direct annealing of melamine is also conducted. As expected, nothing is left in the porcelain boat (Figure S1, Supporting Information). Instead, yellow powders are observed at the end of the tube furnace, which should be g-C$_3$N$_4$, a thermal condensation product of melamine.[30]

Fourier-transform infrared (FTIR) spectroscopy is used to investigate the structural variation of the samples
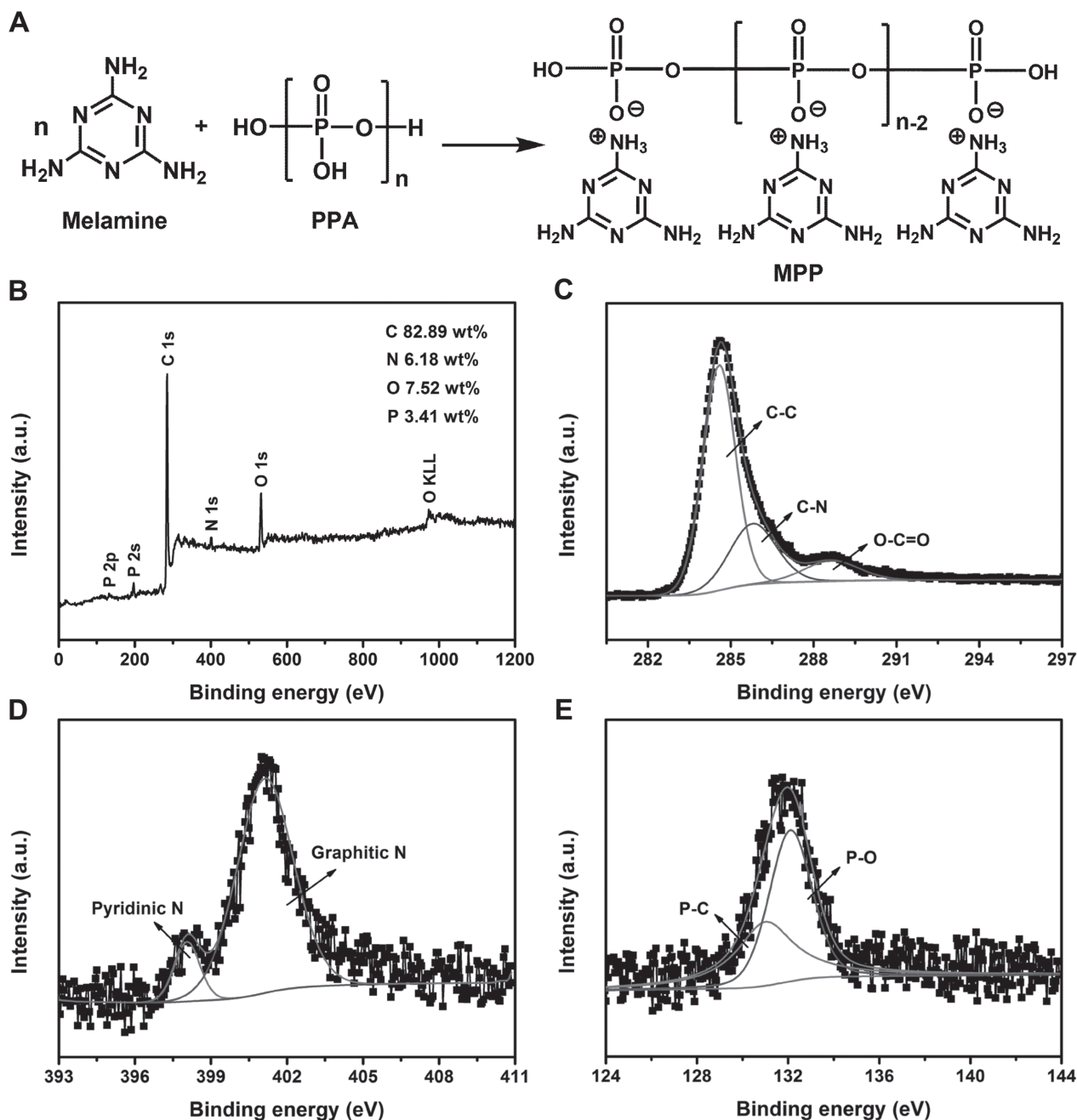
Figure 1. A) Bottom-up synthesis of NPHPC precursor, known as MPP. B) XPS survey spectrum of NPHPC-900. C) High-resolution C 1s XPS spectrum of NPHPC-900 shows the C—C peak at 284.5 eV, C—N peak at 285.8 eV, and O—C=O peak at 288.6 eV. D) High-resolution N 1s XPS spectrum of NPHPC-900. E) High-resolution P 2p XPS spectrum of NPHPC-900 reveals the presence of P—C (130.9 eV) and P—O (132.1 eV) bonds.

(Figure S2, Supporting Information). Melamine shows several characteristic absorption peaks of υ_{N-H} (3468 and 3415 cm^{-1}), δ_{N-H} (3334, 3127, and 1651 cm^{-1}), $\upsilon_{C=N}$ (1547 cm^{-1}), υ_{C-N} (1437 cm^{-1}), and $\upsilon_{triazine}$ (1025 cm^{-1}).[31] In the spectrum of MPP, there is a substantial blue shift for υ_{N-H} peak (3382 cm^{-1}) and two additional peaks corresponding to $\upsilon_{NH3}+$ peak (1512 cm^{-1}) and υ_{P-O} peak (964 cm^{-1}) appear, confirming the successful reaction between melamine and PPA.[32,33] In contrast, the FTIR signals for the above mentioned functional groups become weaker and even disappeared in NPHPC-700, NPHPC-800, and NPHPC-900, which

are attributed to the pyrolysis induced dehydration, fragmentation and aromatization reactions. In another aspect, pyrolysis also promotes new absorption peaks of $\upsilon_{C\equiv N}$ (2202 cm^{-1}), υ_{O-H} (3452 cm^{-1}), $\upsilon_{C=C}$ (1588 cm^{-1}), and υ_{C-O} (1252 cm^{-1}). Some thermally unstable chemical bonds (e.g., C≡N bond) may further decompose and rearrange into aromatic rings containing N and P atoms. X-ray photoelectron spectroscopy (XPS) characterizations are employed to further probe the chemical statue of the surface functional species in NPHPC. C, O, N, and P signals can be distinctly identified from the XPS survey spectra of NPHPC materials (Figure 1B and

Figure S3, Supporting Information), evidencing the successful incorporation of N and P into the carbon matrix.[8,34] However, NPHPC-700 and NPHPC-800 exhibit significant peak shifts associated with the charging effect in comparison with NPHPC-900, which suggests their poor conductivity resulting from the low carbonization degree.[35] This could also be supported by the color change of samples at different pyrolysis temperatures (as shown in Figure S1 in the Supporting Information). The N and P elemental content in NPHPC-900 is measured to be 6.18 and 3.41 wt%, respectively. Oxygen signal should be ascribed to thermally stable oxygen-containing functional groups in NPHPC. High-resolution C 1s spectrum of NPHPC-900 (Figure 1C) is fitted into three peaks corresponding to C−C (284.6 eV), C−N (285.8 eV), and O−C=O (288.6 eV),[8,36] respectively. Deconvolution of high-resolution N 1s spectrum (Figure 1D) reveals two types of N species, i.e. pyridinic N at 398.1 eV and graphitic N at 401.1 eV, both of which are highly favorable for Li ion storage and electrocatalytic oxygen reduction.[37,38] High-resolution spectrum of P 2p (Figure 1E) can be deconvoluted into P–C (130.9 eV) and P–O (132.1 eV) peaks.[39] It is worth mentioning that the presence of these phosphorus species is also beneficial for enhancing the energy storage and conversion performances of the materials.[40,41] In addition, the codoped N and P atoms inevitably introduce structural distortions and vacancies in carbon lattices (Figure S4, Supporting Information), which endows NPHPC-900 rich active sites for electrochemical applications.

The Raman spectrum of NPHPC-900 (Figure S5, Supporting Information) presents two remarkable peaks located at ≈1592 and ≈1344 cm^{-1}, corresponding to G band (E_{2g} mode of graphitic carbon) and D band (defects/disorder activated Raman mode) of carbon-based materials, respectively.[42] On the contrary, the Raman spectra of NPHPC-700 and NPHPC-800 show strong fluorescence signal that arises from incompletely carbonized MPP. X-ray diffraction (XRD) patterns of NPHPC materials (Figure S6, Supporting Information) exhibit a broad peak at 2θ = 20°–25° that belongs to typical carbon-based materials possessing disordered structures.[43] Moreover, the increase of pyrolysis temperature leads to a progressive shift of NPHPC diffraction peak toward a higher degree, indicating an enhanced graphitization state. These results are in good agreement with the XPS (Figure 1B and Figure S3, Supporting Information) and Raman (Figure S5, Supporting Information) analysis, which verify the conversion of MPP to NPHPC. The textural properties of NPHPC-900 are evaluated by N$_2$ adsorption and desorption analysis. NPHPC-900 exhibits a typical type IV N$_2$ adsorption–desorption isotherm with a steep initial uptake (P/P_0 < 0.01) and H3 type hysteresis loop (**Figure 2**A), suggesting the coexistence of hierarchical micropores and mesopores.[44] The Brunauer–Emmett–Teller (BET) surface area of NPHPC-900 reaches up to 1479 m^2 g^{-1} with a total pore volume of 1.95 cm^3 g^{-1}. Additionally, the pore size (D) distribution curve (Figure 2B) reveals a multimodal pore distribution in NPHPC-900, including micropores (D < 2 nm), mesopores (2 < D < 50 nm) and macropores (D > 50 nm).

Figure 3A and Figure S7 in the Supporting Information depict the scanning electron microscopy (SEM)

images of NPHPC samples. With the increase of pyrolysis temperature from 700 to 900 °C, the structure of NPHPC changes distinctly from co-continuous skeletons with isolated pores to 3D networks with interconnected pores. The morphology of NPHPC-900 is constructed by highly curved carbon nanowalls with abundance of surface defects (Figure 3B). Transmission electron microscopy (TEM) images (Figure 3C–D) reveal substantial micropores and mesopores within the carbon nanowalls, which is consistent with BET results (Figure 2). These uniformly distributed pores possibly originate from the decomposition of MPP during thermal annealing process. Such unique structure provides large amounts of active sites and ensures efficient mass transport, which are crucial for energy storage and conversion applications. High-resolution TEM (HRTEM) image (Figure 3E) demonstrates that graphitic carbon layers of NPHPC-900 contain short-range order of sp^2 domains and dislocated defects. Elemental mapping images from the selected area of NPHPC-900 sample show a homogenous distribution of N and P (Figure 3F–I), while energy-dispersive X-ray spectroscopy (Figure S8, Supporting Information) exhibits a comparable doping contents (N: 5.89 wt%, P: 3.56 wt%) with that obtained from XPS.
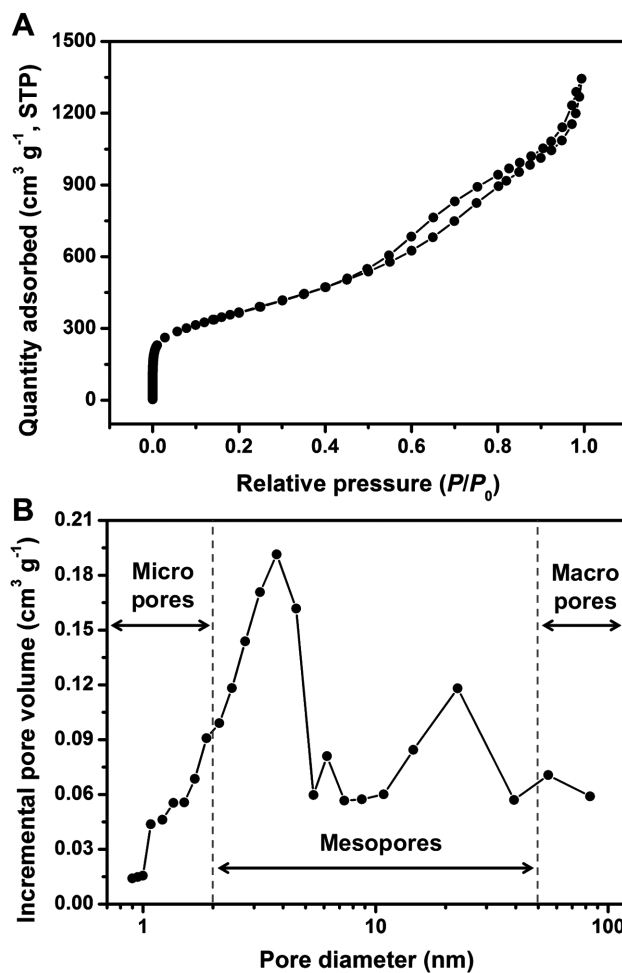
Figure 2. A) N$_2$ adsorption–desorption isotherms of NPHPC-900 at 77 K. B) Pore size distribution (dV/dlog D) of NPHPC-900.
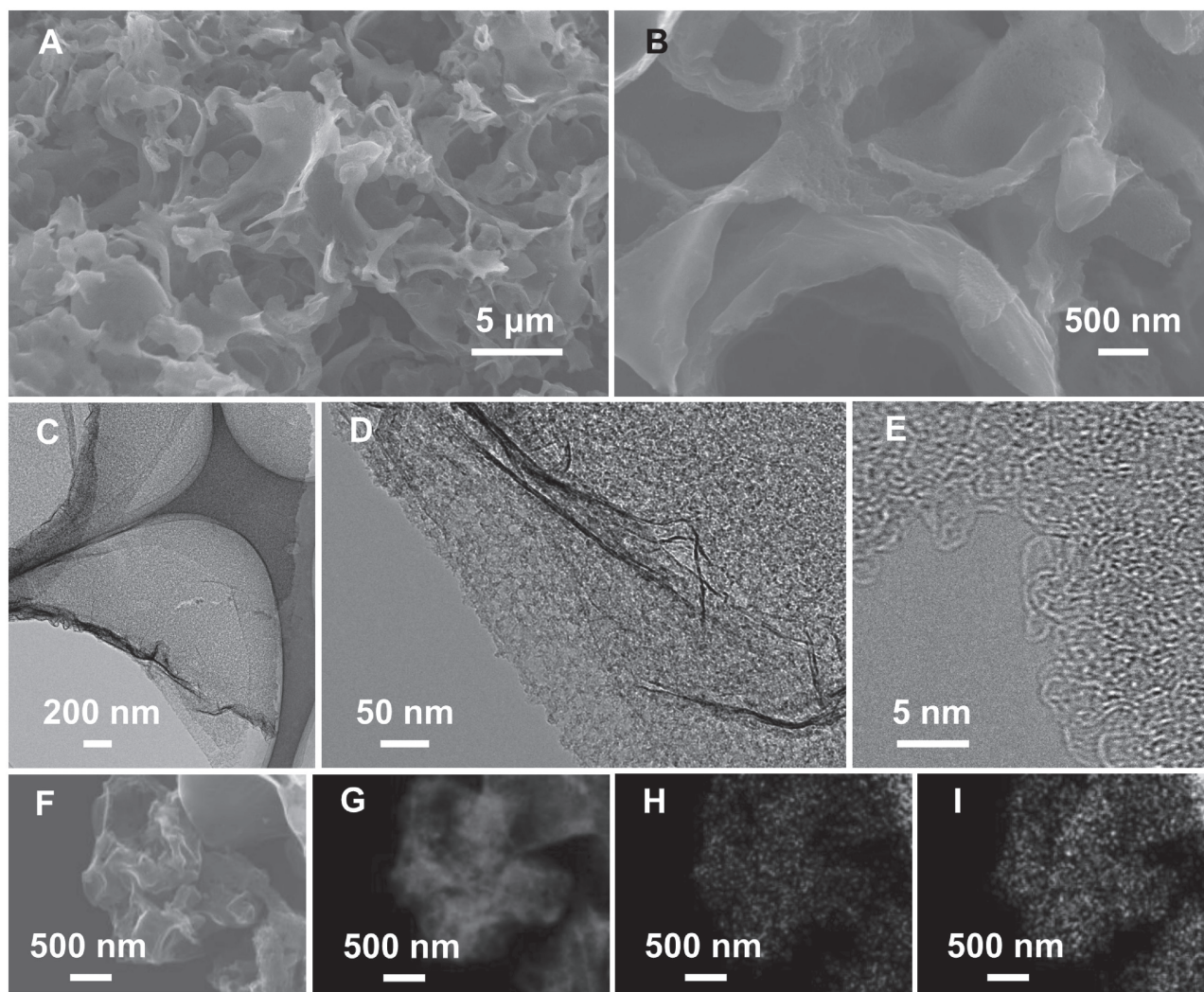
Figure 3. SEM images of NPHPC-900 at A) low and B) high magnifications. C,D) TEM images of NPHPC-900 at different magnifications reveal the presence of substantial micropores and mesopores within the carbon nanowalls. E) HRTEM image of NPHPC-900. F) SEM image and the corresponding elemental mapping images of G) carbon, H) nitrogen, and I) phosphorus, indicating the homogenous distribution of N and P over the entire NPHPC-900 nanostructure.

2.2. Electrochemical Performance for LIBs

Li storage properties of NPHPC are evaluated by using standard coin-type cells. As shown in **Figure 4**A and Figure S9A,B in the Supporting Information, the cyclic voltammetry (CV) curves of NPHPC samples belong to typical carbon-based anodes.[8,43] Two pronounced irreversible peaks are observed during the first cathodic scan. The peak at ≈0.6 V is assigned to the formation of a solid electrolyte interphase (SEI) layer on the surface of the electrode caused by electrolyte decomposition,[45] while the peak at ≈1.3 V is possibly derived from Li insertion into hydrogen atom-bonded carbon lattices.[46] Two additional reduction peaks at ≈1.0 and ≈1.6 V are observed in NPHPC-700 and NPHPC-800, which may come from the irreversible reactions of Li with functional groups remained at lower pyrolysis temperature (as shown in Figures S2 and S3 in the Supporting Information).[46,47] The anodic peak existed in all samples at ≈1.1 V may be associated with Li extraction from pores

and defective sites of NPHPC materials.[48] The overlapped CV curves from the second cycle suggest a good stability and reversibility of all these materials. Figure 4B shows the first three charge–discharge curves of NPHPC-900 electrode at a current density of 0.5 C (1 C = 372 mA g^{-1}). In the first discharge curve, a voltage plateau related to SEI formation is observed at 0.6–1.0 V and disappears in the subsequent discharge process, which matches well with the CV curves. The NPHPC-900 electrode delivers an initial reversible capacity of 1044 mAh g^{-1} that is ≈3 times larger than the theoretical value of graphite (372 mAh g^{-1}). Despite a large irreversible capacity in first cycle, the electrochemical reactions gradually become reversible and stable upon cycling, leading to a significantly increased coulombic efficiency of over 92% in the third cycle.

Figure 4C presents the cycling performance of the NPHPC-900 electrode at a current density of 0.5 C. A high reversible capacity of 1073 mAh g^{-1} with a coulombic efficiency of 99.3% is still retained after 300 cycles. Nevertheless,
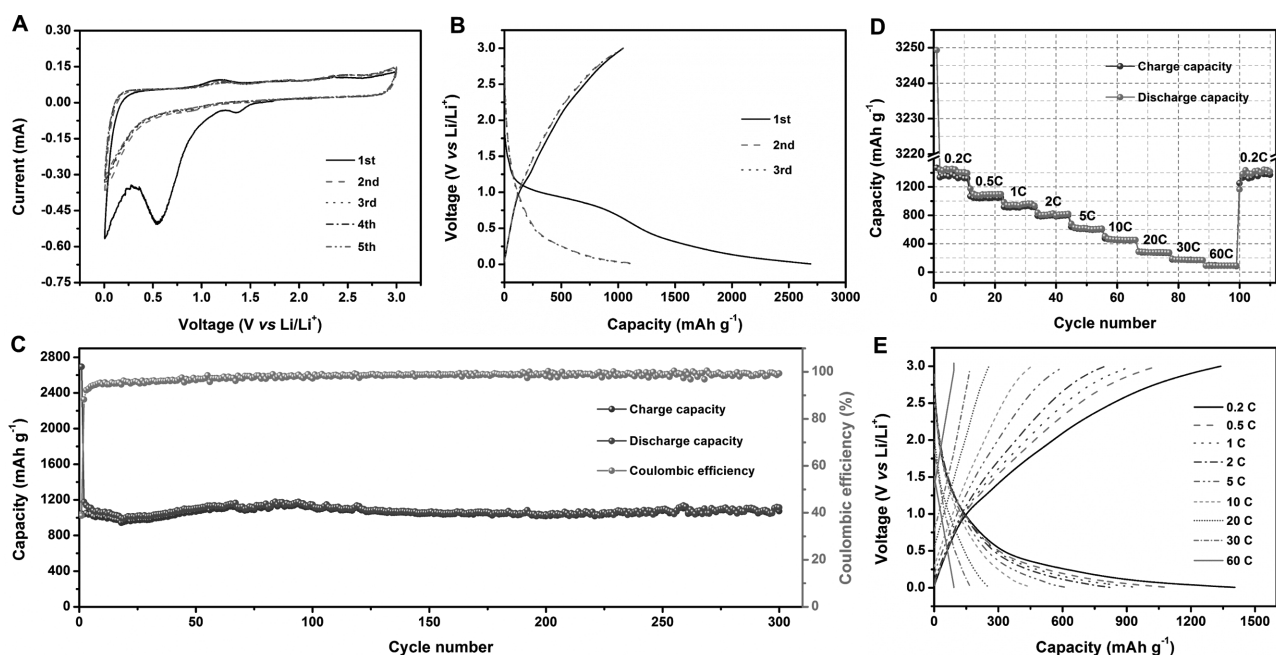
Figure 4. Electrochemical performances of NPHPC-900 anode for LIBs. A) CV profiles of the NPHPC-900 electrode at a scan rate of 0.5 mV s^{-1} over the potential window of 0.005–3 (vs Li/Li$^+$). B) Galvanostatic charge–discharge curves of NPHPC-900 electrode for the first three cycles at a current density of 0.5 C. C) Cycling performance and coulombic efficiency of NPHPC-900 electrode tested at a current density of 0.5 C. D) Rate performance and E) galvanostatic charge–discharge curves of NPHPC-900 electrode cycled at various current densities ranging from 0.2 to 60 C.

NPHPC-700 and NPHPC-800 electrodes exhibit low Li storage capacities because of their low carbonization state (Figure S9C,D, Supporting Information). The rate performance of NPHPC-900 electrode is tested at programmed C rates (Figure 4D,E). With the current density increasing stepwise from 0.2 to 0.5, 1, 2, 5, 10, 20, and 30 C, NPHPC-900 electrode remains capable of delivering a reversible capacity of 1321, 1054, 926, 785, 606, 454, 277, and 176 mAh g^{-1}, respectively. Even at an extremely high current rate of 60 C (corresponding to a full charge time of 16 s), the electrode still achieves a high reversible capacity of 98 mAh g^{-1}. Importantly, the good capacity recovery after the current rate switching back to 0.2 C demonstrates the excellent rate capability of the electrode. The fascinating performance of NPHPC-900 is definitely superior to that of previously reported carbon-based anodes, such as P-doped graphene,[40] N-doped carbon nanofibers,[10] FeCl$_3$-intercalated graphite,[49] porous carbon,[50] and carbon nanotubes.[51] Such extraordinary results are likely to originate from the unique structural feature of NPHPC-900 and the synergistic effect of N and P codopants (see following discussion for details). Further work is under way to optimize the gravimetric/volumetric capacity, that is, to upgrade the energy density of the material.

2.3. Electrocatalytic Performance for ORR

Electrocatalytic ORR activity of NPHPC-900 in comparison with commercial Pt/C catalyst (Vulcan, 20 wt%, Fuel Cell Earth) is evaluated in N$_2$- and O$_2$-saturated 0.1 mol L^{-1} KOH solutions. Pt/C loading amount is optimized to give the best performance. **Figure 5**A reproduces the CV curves of NPHPC-900 and commercial Pt/C, showing distinct cathodic reduction

peaks in O$_2$-saturated KOH solution, whereas quasi-rectangular voltammograms in N$_2$-saturated electrolyte. The ORR peak of NPHPC-900 is centered at 0.77 V versus reversible hydrogen electrode (RHE), close to that of commercial Pt/C (0.83 V), indicative of its prominent electrocatalytic activity. To further explore ORR performance and kinetics of NPHPC-900, linear sweep voltammetry (LSV) is further performed on a rotating disk electrode (RDE) at different rotation speeds (Figure 5B). An onset potential of 0.88 V and a half-wave potential of 0.79 V are measured, which outperform the recently reported advanced metal-free electrocatalysts[52–54] and even previously reported carbonaceous catalysts with metals.[55,56] The corresponding Koutecky–Levich (K–L) plots (J^{-1} vs w$^{-0.5}$) at different potential show good linear relationships with good parallelity (Figure 5C), indicating a first-order reaction kinetics. The electron transfer number (n) of each O$_2$ molecule involved in the ORR process is calculated to be 3.5–4.0 over the potential range of 0.16–0.66 V, suggesting a quasi-four-electron ORR process.

Since durability is a critical parameter for practical applications of electrocatalysts, the stability of NPHPC-900 is evaluated by chronoamperometric measurements at a constant voltage of 0.56 V in O$_2$-saturated 0.1 mol L^{-1} KOH solution with a rotation speed of 1600 rpm (Figure 5D). Remarkably, NPHPC-900 displays a slow current attenuation (current retention 89.8%) during a 20 000 s continuous test, far superior to that of commercial Pt/C (82.7%).[52,57] To study the fuel crossover effect, the electrocatalyst is exposed to the electrolyte containing 2% (v/v) methanol (inset of Figure 5D). In comparison with the significant methanol oxidation on Pt/C electrode, NPHPC-900 exhibits negligible current response upon the addition of methanol, which demonstrates NPHPC-900 a superior methanol tolerance.[40]
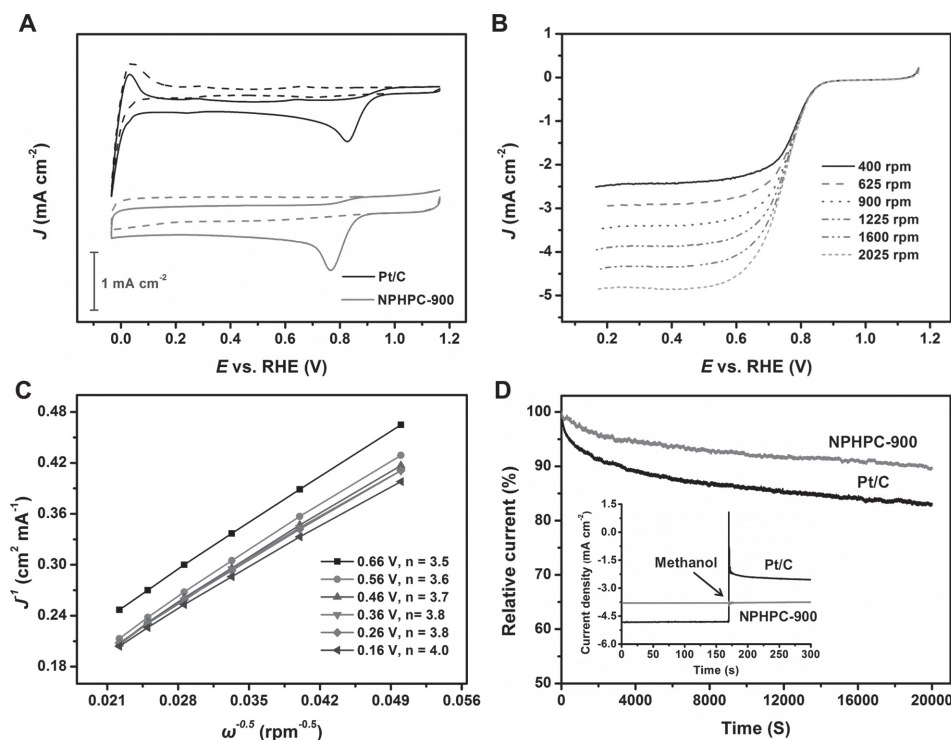
Figure 5. Electrocatalytic performances of NPHPC-900 for ORR. A) CV curves of NPHPC-900 and commercial Pt/C on glassy carbon electrodes in N_2-saturated (dash line) and O_2-saturated (solid line) 0.1 mol L^{-1} KOH solutions with a sweep rate of 10 mV s^{-1}. B) RDE voltammograms of NPHPC-900 in O_2-saturated 0.1 mol L^{-1} KOH with a sweep rate of 5 mV s^{-1} at various rotation rates. C) K–L plots at different potentials for NPHPC-900. D) Chronoamperometric response of NPHPC-900 and commercial Pt/C for 20 000 s at 0.56 V in O_2-saturated 0.1 mol L^{-1} KOH solution (rotation rate: 1600 rpm). The inset in (D) shows the chronoamperometric response of the electrodes with addition of 2% (v/v) methanol under the same condition.

These results indicate the application potential of NPHPC-900 in metal–air batteries and fuel cells.

The exceptional performance of NPHPC-900 for energy storage and conversion applications benefits from the following synergistic effects: First, pyrolysis induces a random assembly of the resulting highly curved carbon nanowalls, leading to the generation of a 3D porous structure. This continuous 3D network not merely renders sufficient contact areas between the electrolyte and active material but also serves as a robust matrix for fast charge transfer reaction. Second, the large BET surface area and hierarchically porous structure exactly satisfy the criteria for electrochemical energy storage and conversion devices. With that, large surface area guarantees sufficient exposure and improved accessibility of electrochemical active sites; micropores provide abundant active sites; mesopores ensure efficient mass transport, and macropores facilitate the penetration and diffusion of electrolyte. Third, the different electronegativities between the codopants (N (3.04) and P (2.19)) and C (2.55) synergistically induce topological defects and structural distortions in the carbon network, which are highly active sites for electrochemical reactions. Furthermore, the codopants in NPHPC can also greatly increase the conductivity that is beneficial for fast electron transportation. Finally, as normally observed in the organic precursor derived carbon materials,[29,58] the thermally stable functional groups and residual hydrogen atoms in the carbon network further contribute to its excellent electrochemical performances.

3. Conclusion

In summary, we present a versatile chemical strategy to prepare novel carbon-based materials through a molecular-level design principle. The resulting NPHPC has a hierarchically porous structure with a large BET surface area, and a high N (6.18 wt%) and P (3.41 wt%) content. The peculiar structure and synergistic effect of N and P codopants confer NPHPC remarkable electrochemical performances for both LIBs and ORR. Our NPHPC-based LIB anode exhibits a high reversible capacity of 1321 mAh g^{-1} at a low rate of 0.2 C with high rate capability (98 mAh g^{-1} at 60 C) as well as good cyclability (300 cycles with negligible capacity decade). The electrocatalytic ORR performances of NPHPC are comparable to that of commercial Pt/C catalyst with excellent long-term stability and methanol tolerance. The strategy developed here is efficient and practically meaningful because of its simplicity, scalability, and low cost. We believe that this synthetic protocol will open up a new avenue for the development of advanced carbon-based materials for future sustainable energy systems.

4. Experimental Section

Preparation of NPHPC Materials: 5.04 g melamine (Sigma-Aldrich) was dissolved in 400 mL water at 80 °C with vigorous stirring. Then, 5 mL (≈10 g) PPA (Sigma-Aldrich) was added by

using a syringe, immediately resulting in a milk-like suspension. After further stirring at 80 °C for 2 h, the mixture was centrifuged and then thoroughly washed with deionized water before drying in a thermostatic oven at 90 °C for 12 h. The NPHPC powder was obtained by pyrolysis of the white MPP precipitate at the predetermined temperature (700, 800, and 900 °C) in a tubular furnace under argon atmosphere for 2 h (heating rate: 5 °C min^{-1}, flow rate: 100 cm^3 min^{-1}). Considering the higher annealing temperature (>900 °C) will result in lower yield, lower heteroatom doping level, and smaller surface area associated with the collapse of pores, and consequently leads to poor electrochemical performance.[37] The authors finally chose 900 °C as the optimal temperature.

Characterization: XPS was measured on an ESCALAB MK II X-ray photoelectron spectrometer (VG Scientific Ltd, UK) equipped with a monochromatic Al Kα X-ray source. SEM and elemental mapping were performed on a Zeiss Auriga Dual-Beam FIB/SEM (North Chesterfield, VA, USA) system. TEM was carried out on a JEM-2100 transmission electron microscope (JEOL Ltd, Japan). FTIR was recorded in the range of 4000−600 cm^{-1} on a NEXUS 670 spectrometer (Thermo Scientific, Waltham, MA, USA) with samples pressed into KBr pellets. Raman spectra were obtained with a 532 nm laser as the excitation source (WITEC, Germany). XRD was conducted on a D8 Advance diffractometer (Bruker, Germany) using a Cu Kα radiation. N$_2$ adsorption and desorption analysis was done with a Micromeritics ASAP 2020 instrument (Norcross, GA, USA) at 77 K. The pore size distribution was obtained from the adsorption branch of the isotherm using Barrett–Joyner–Halenda method.

Electrochemical Characterizations: Electrodes for Li storage were prepared by casting the slurry onto the Cu foil current collector, and then dried in a vacuum oven at 100 °C overnight. The slurry was fabricated by combining 80 wt% active material, 10 wt% polyvinylidene difluoride, and 10 wt% acetylene black in *N*-methyl-2-pyrrolidone. Circular electrodes (12 mm in diameter) were punched out by a punching machine, and weighed using a 0.01 mg highly accurate electronic balance. The mass loaded on each electrode was controlled to be 1.0–1.5 mg, and the specific capacities were all calculated based on the weight of active materials. Electrochemical performances of the electrode materials were evaluated by using standard coin-type cells (CR2032) with pure Li foil as anode. The electrolyte was 1 mol L^{-1} LiPF$_6$ dissolved in a 1:1 (w/w) mixture of ethylene carbonate and dimethyl carbonate. Cells were assembled in an argon-filled glove box with oxygen and moisture levels below 0.1 ppm. Galvanostatic cycling was performed on a NEWARE multichannel battery testing system, CV was carried out on a CHI 760D electrochemical workstation.

The electrocatalytic activities of NPHPC-900 were measured using CHI 760D electrochemical workstation with a conventional three-electrode cell configuration. A glassy carbon disk (5 mm in diameter) was used as the substrate for loading electrode materials, with a Pt wire (0.5 mm in diameter) and Ag/AgCl serving as counter and reference electrodes, respectively. All potentials referring to RHE were converted from the measured potentials versus Ag/AgCl electrode according to Nernst equation: $E_{RHE} = E_{Ag/AgCl} + E^{\varnothing}_{Ag/AgCl} + 0.059$ pH.[1,8,59] For the preparation of working electrodes, 5 mg NPHPC-900 was first dispersed into 1 mL solution (0.9 mL deionized water and 0.1 mL 5 wt% Nafion aqueous solution) under sonication. 20 µL of the as-formed homogenous catalyst ink was then uniformly deposited onto the prepolished

glassy carbon electrodes, and fully dried at 50 °C. ORR measurements were conducted in an O$_2$-saturated 0.1 mol L^{-1} KOH solution at room temperature. LSV curves were recorded on the rotating disc electrode with a scan rate of 10 mV s^{-1} at various rotating speeds ranging from 400 to 2025 rpm. For comparison, the ORR performance of commercial Pt/C was also conducted using the same setup. For all the ORR measurements, the areal loading of catalyst is ≈0.5 mg cm^{-2} for NPHPC-900 and 0.127 mg cm^{-2} for Pt/C, which is optimized to give the best performance. Onset potential is determined as the starting potential of ORR at which there is an increase of current density in CV curve obtained in O$_2$ saturated electrolyte solution as compared to that obtained in N$_2$ saturated electrolyte. Half-wave potential is determined as a potential at which the current density in LSV curve is equal to one half of limiting diffusion current density.

Supporting Information

Supporting Information is available from the Wiley Online Library or from the author.

[1] F. Bonaccorso, L. Colombo, G. Yu, M. Stoller, V. Tozzini, A. C. Ferrari, R. S. Ruoff, V. Pellegrini, *Science* **2015**, *347*, 1246501.

[2] D. Larcher, J. M. Tarascon, *Nat. Chem.* **2015**, *7*, 19.

[3] J. Suntivich, H. A. Gasteiger, N. Yabuuchi, H. Nakanishi, J. B. Goodenough, Y. Shao-Horn, *Nat. Chem.* **2011**, *3*, 546.

[4] L. Dai, Y. Xue, L. Qu, H. J. Choi, J. B. Baek, *Chem. Rev.* **2015**, *115*, 4823.

[5] W. Ai, J. H. Zhu, J. Jiang, D. L. Chao, Y. L. Wang, C. F. Ng, X. L. Wang, C. Wu, C. M. Li, Z. X. Shen, W. Huang, T. Yu, *2D Mater.* **2015**, *2*, 014005.

[6] M. V. Reddy, G. V. Subba Rao, B. V. R. Chowdari, *Chem. Rev.* **2013**, *113*, 5364.

[7] C. Wei, L. Yu, C. Cui, J. Lin, C. Wei, N. Mathews, F. Huo, T. Sritharan, Z. Xu, *Chem. Commun.* **2014**, *50*, 7885.

[8] W. Ai, Z. Luo, J. Jiang, J. Zhu, Z. Du, Z. Fan, L. Xie, H. Zhang, W. Huang, T. Yu, *Adv. Mater.* **2014**, *26*, 6186.

[9] Z. Li, Z. Xu, X. Tan, H. Wang, C. M. B. Holt, T. Stephenson, B. C. Olsen, D. Mitlin, *Energy Environ. Sci.* **2013**, *6*, 871.

[10] B. Zhang, Y. Yu, Z. L. Xu, S. Abouali, M. Akbari, Y. B. He, F. Kang, J. K. Kim, *Adv. Energy Mater.* **2014**, *4*, 1301448.

[11] Y. Chen, X. Li, K. Park, J. Song, J. Hong, L. Zhou, Y. W. Mai, H. Huang, J. B. Goodenough, *J. Am. Chem. Soc.* **2013**, *135*, 16280.

[12] X. Wang, G. Sun, P. Routh, D. H. Kim, W. Huang, P. Chen, *Chem. Soc. Rev.* **2014**, *43*, 7067.

[13] Z. S. Wu, A. Winter, L. Chen, Y. Sun, A. Turchanin, X. Feng, K. Mullen, *Adv. Mater.* **2012**, *24*, 5130.

[14] J. Zhang, L. Qu, G. Shi, J. Liu, J. Chen, L. Dai, *Angew. Chem. Int. Ed.* **2016**, *55*, 2230.

[15] R. Li, Z. Wei, X. Gou, *ACS Catal.* **2015**, *5*, 4133.

[16] J. Zhou, J. Lian, L. Hou, J. Zhang, H. Gou, M. Xia, Y. Zhao, T. A. Strobel, L. Tao, F. Gao, *Nat. Commun.* **2015**, *6*, 8503.

[17] Y. Ito, W. Cong, T. Fujita, Z. Tang, M. Chen, *Angew. Chem. Int. Ed.* **2015**, *54*, 2131.

[18] J. Zhang, Z. Zhao, Z. Xia, L. Dai, *Nat. Nanotechnol.* **2015**, *10*, 444.

[19] Y. P. Zhu, Y. P. Liu, Z. Y. Yuan, *Chem. Commun.* **2016**, *52*, 2118.

[20] Z. Xu, X. Zhuang, C. Yang, J. Cao, Z. Yao, Y. Tang, J. Jiang, D. Wu, X. Feng, *Adv. Mater.* **2016**, *28*, 1981.

[21] J. Tang, J. Liu, C. Li, Y. Li, M. O. Tade, S. Dai, Y. Yamauchi, *Angew. Chem. Int. Ed.* **2015**, *54*, 588.

[22] X. Liu, M. Antonietti, *Adv. Mater.* **2013**, *25*, 6284.

[23] W. Gu, M. Sevilla, A. Magasinski, A. B. Fuertes, G. Yushin, *Energy Environ. Sci.* **2013**, *6*, 2465.

[24] H. Nishihara, T. Kyotani, *Adv. Mater.* **2012**, *24*, 4473.

[25] J. Wang, S. Kaskel, *J. Mater. Chem.* **2012**, *22*, 23710.

[26] M. Molina-Sabio, F. RodRiguez-Reinoso, F. Caturla, M. J. Selles, *Carbon* **1995**, *33*, 1105.

[27] M. Jagtoyen, F. Derbyshire, *Carbon* **1998**, *36*, 1085.

[28] Y. Zhu, S. Murali, M. D. Stoller, K. J. Ganesh, W. Cai, P. J. Ferreira, A. Pirkle, R. M. Wallace, K. A. Cychosz, M. Thommes, D. Su, E. A. Stach, R. S. Ruoff, *Science* **2011**, *332*, 1537.

[29] H. W. Liang, X. Zhuang, S. Bruller, X. Feng, K. Mullen, *Nat. Commun.* **2014**, *5*, 4973.

[30] M. Groenewolt, M. Antonietti, *Adv. Mater.* **2005**, *17*, 1789.

[31] B. Jurgens, E. Irran, J. Senker, P. Kroll, H. Muller, W. Schnick, *J. Am. Chem. Soc.* **2003**, *125*, 10288.

[32] N. C. Polfer, J. Oomens, S. Suhai, B. Paizs, *J. Am. Chem. Soc.* **2007**, *129*, 5887.

[33] G. Xu, I. A. Aksay, J. T. Groves, *J. Am. Chem. Soc.* **2001**, *123*, 2196.

[34] M. J. Kim, I. Y. Jeon, J. M. Seo, L. Dai, J. B. Baek, *ACS Nano* **2014**, *8*, 2820.

[35] H. S. Shin, H. C. Choi, Y. Jung, S. B. Kim, H. J. Song, H. J. Shin, *Chem. Phys. Lett.* **2004**, *383*, 418.

[36] W. Ai, X. Cao, Z. Sun, J. Jiang, Z. Du, L. Xie, Y. Wang, X. Wang, H. Zhang, W. Huang, T. Yu, *J. Mater. Chem. A* **2014**, *2*, 12924.

[37] W. Ai, J. Jiang, J. Zhu, Z. Fan, Y. Wang, H. Zhang, W. Huang, T. Yu, *Adv. Energy Mater.* **2015**, *5*, 1500559.

[38] Y. Su, H. Jiang, Y. Zhu, X. Yang, J. Shen, W. Zou, J. Chen, C. Li, *J. Mater. Chem. A* **2014**, *2*, 7281.

[39] M. Latorre-Sanchez, A. Primo, H. Garcia, *Angew. Chem. Int. Ed.* **2013**, *52*, 11813.

[40] C. Zhang, N. Mahmood, H. Yin, F. Liu, Y. Hou, *Adv. Mater.* **2013**, *25*, 4932.

[41] D. S. Yang, D. Bhattacharjya, S. Inamdar, J. Park, J. S. Yu, *J. Am. Chem. Soc.* **2012**, *134*, 16127.

[42] W. Ai, W. Zhou, Z. Du, C. Sun, J. Yang, Y. Chen, Z. Sun, S. Feng, J. Zhao, X. Dong, W. Huang, T. Yu, *Adv. Funct. Mater.* **2016**, DOI: 10.1002/adfm.201603603.

[43] Y. Mao, H. Duan, B. Xu, L. Zhang, Y. Hu, C. Zhao, Z. Wang, L. Chen, Y. Yang, *Energy Environ. Sci.* **2012**, *5*, 7950.

[44] Y. Tao, H. Kanoh, L. Abrams, K. Kaneko, *Chem. Rev.* **2006**, *106*, 896.

[45] N. A. Kaskhedikar, J. Maier, *Adv. Mater.* **2009**, *21*, 2664.

[46] Y. Matsumura, S. Wang, J. Mondori, *J. Electrochem. Soc.* **1995**, *142*, 2914.

[47] J. Xu, I. Y. Jeon, J. M. Seo, S. Dou, L. Dai, J. B. Baek, *Adv. Mater.* **2014**, *26*, 7317.

[48] W. Ai, Z. Du, Z. Fan, J. Jiang, Y. Wang, H. Zhang, L. Xie, W. Huang, T. Yu, *Carbon* **2014**, *76*, 148.

[49] F. Wang, J. Yi, Y. Wang, C. Wang, J. Wang, Y. Xia, *Adv. Energy Mater.* **2014**, *4*, 1300600.

[50] P. Adelhelm, Y. S. Hu, L. Chuenchom, M. Antonietti, B. M. Smarsly, J. Maier, *Adv. Mater.* **2007**, *19*, 4012.

[51] M. Li, Y. Wu, F. Zhao, Y. Wei, J. Wang, K. Jiang, S. Fan, *Carbon* **2014**, *69*, 444.

[52] L. Hao, S. Zhang, R. Liu, J. Ning, G. Zhang, L. Zhi, *Adv. Mater.* **2015**, *27*, 3190.

[53] I. Y. Jeon, S. Zhang, L. Zhang, H. J. Choi, J. M. Seo, Z. Xia, L. Dai, J. B. Baek, *Adv. Mater.* **2013**, *25*, 6138.

[54] P. Chen, T. Y. Xiao, Y. H. Qian, S. S. Li, S. H. Yu, *Adv. Mater.* **2013**, *25*, 3192.

[55] Z. S. Wu, L. Chen, J. Liu, K. Parvez, H. Liang, J. Shu, H. Sachdev, R. Graf, X. Feng, K. Mullen, *Adv. Mater.* **2014**, *26*, 1450.

[56] Y. Zhao, K. Watanabe, K. Hashimoto, *J. Am. Chem. Soc.* **2012**, *134*, 19528.

[57] Y. Liang, Y. Li, H. Wang, J. Zhou, J. Wang, T. Regier, H. Dai, *Nat. Mater.* **2011**, *10*, 780.

[58] J. R. Dahn, T. Zheng, Y. Liu, J. S. Xue, *Science* **1995**, *270*, 590.

[59] Y. Hou, T. Huang, Z. Wen, S. Mao, S. Cui, J. Chen, *Adv. Energy Mater.* **2014**, *4*, 1400337.